Modulating dual carrier-transfer channels and band structure in carbon nitride to amplify ROS storm for enhanced cancer photodynamic therapy

Meixian Liu [a],[*],[1], Yuan Zhang [a],[1], Fa Jiang [c], Wenzhao Guan [d], Jing Cui [e], Liwei Liu [f], Qingpeng Xie [a], Jia Wang [a], Shuyun Xue [a], Jiawen Gu [a], Zhanfeng Zheng [b], Xiuyun Ren [a],[**], Xing Wang [a],[***]

[a] School and Hospital of Stomatology, Shanxi Medical University, Taiyuan, 030001, China
[b] State Key Laboratory of Coal Conversion, Institute of Coal Chemistry, Chinese Academy of Sciences, Taiyuan, 030001, China
[c] College of Biomedical Engineering, Taiyuan University of Technology, Taiyuan, 030600, China
[d] Second Hospital of Shanxi Medical University, Taiyuan, 030001, China
[e] The Third Hospital of Shanxi Medical University, Taiyuan, 030032, China
[f] First Hospital of Shanxi Medical University, Taiyuan, 030001, China

ARTICLE INFO

ABSTRACT

Graphite carbon nitride (CN) eliminates cancer cells by converting H_2O_2 to highly toxic •OH under visible light. However, its in vivo applications are constrained by insufficient endogenous H_2O_2, accumulation of OH^- and finite photocarriers. We designed Fe/N_V-CN, co-modified CN with nitrogen vacancies (N_V) and ferric ions (Fe^{3+}). N_V and Fe^{3+}, not only adjust the band structure of CN through quantum confinement effect and the altered coupled oscillations of atomic orbitals to facilitates •OH production by oxidizing OH^-, but also construct dual carrier-transfer channels for electrons and holes to respective active sites by introducing stepped electrostatic potential and shortening three-electron bonds, thereby involving more carriers in •OH production. Fe/N_V-CN, the novel reactor, effectually produces vast •OH under illumination by expanding OH^- as the raw material of •OH and augmenting carriers at active sites, which induces cancer cell apoptosis by disrupting mitochondrial function for significant shrinkage of Cal27 cell-induced tumor under illumination. This work provides not only an effective photosensitizer avoiding the accumulation of OH^- for cancer therapy but also a novel strategy by constructing dual carrier-transfer channels on semiconductor photosensitizers for improving the therapeutic effect of photodynamic therapy.

1. Introduction

Despite considerable advances in treatment, cancer is still responsible for one in six deaths worldwide [1]. Treatment modality is pivotal for survival rate and life quality of cancer patients. Hydroxyl radicals (•OH), characterized by a standard redox potential at 2.8 V, have the ability to rapidly destroy macromolecular entities and cause dysfunction in subcellular organelles. This attribute positions them as one of the most powerful weapon for effectively eliminating cancer cells [2]. Capitalizing on the overexpression of hydrogen peroxide (H_2O_2) in tumor, the conversion of H_2O_2 into •OH for cancer cell eradication represents a strategy that addresses the serious side effects and drug resistance commonly associated with radiotherapy and chemotherapy. Of note, the short half-life of •OH guarantees a high level of tumor specificity [3,4]. Chemodynamic therapy (CDT) involves the conversion of H_2O_2 to •OH and hydroxyl ion (OH^-) based on Fenton (Fe^{2+}) or Fenton-like agents (variable valence metal ions such as Cu^+, Mn^{2+}, Co^{2+}, etc.). Challenge exists for CDT in the form of adverse effects associated with high concentrations of Fenton agents on normal tissue [5]. Photodynamic therapy (PDT), a non-invasive therapeutic technique, by contrast, offers convenient and spatiotemporal control for site-directed release of deleterious free radicals. This technique exhibits

---

significant potential in anticancer therapy, particularly for superficial tumor [4].

PDT operates by reducing H_2O_2 to $\bullet OH$ through photoinduced electrons (e^-) on photosensitizers (Equation 1) [6]. Typical organic photosensitizers (e.g. porphyrins, chlorins and phthalocyanine) exhibit instability characterized by issues such as photobleaching or aggregating [7]. Semiconductor nano-photosensitizers (NPSs) with superior aqueous dispersity and robust stability play a predominant role in PDT. Among numerous semiconductor materials, including metal oxide, metal sulfide, phosphorus and carbon-based NPSs, graphite carbon nitride (CN) stands out for remarkable biocompatibility and finds applications in various biomedical fields, including biosensing, bioimaging and cancer therapy [8,9]. The visible-light-active ability of CN allows it to avoid poor tissue penetration, anaphylaxis and melanin production under ultraviolet (UV), and skin heat injury under near infrared light (NIR) during superficial tumor therapy [10]. Of note, the easily adjustable surface and band structure of CN render it promising for addressing various challenges encountered in cancer treatment [11].

Practically, the insufficient endogenous H_2O_2 in tumor environment (TME), accumulation of by-product OH^-, and finite photocarriers, collectively constrain the in vivo cancer PDT effect of pristine CN [12]. Considerable efforts in structure design of CN have been devoted for better therapeutic effect. For instance, assembling CN with other materials possessing photothermal effect (carbon nanosheet or graphene quantum dot) for combining photoinduced thermal therapy (PTT) and PDT [13,14]; extending the light absorption range of CN (carbon dots or polydopamine nanosphere decorated CN) or constructing heterojunction with other semiconductors (TiO_2 and Bi_2WO_6) for adequate photocarriers [15,16]; supplying extra H_2O_2 via the reaction of water and oxygen [17,18]. However, these strategies increase drug complexity and biosecurity risks, and do not address the accumulation of OH^- [19]. The accumulated OH^- not only inhibit the reduction of H_2O_2, but also lead to therapy resistance risk by triggering autophagy of cancer cells [20,21]. Simple modification strategies of CN capable of meeting above three matters remain elusive.

If abundant e^- and photoinduced holes (h^+) apace migrate to respective active sites to reduce H_2O_2 (Equation (1)) and oxidize OH^- (Equation (2)) to produce $\bullet OH$, the above three problems will be easily solved. However, the band structure of pristine CN is suitable for $H_2O_2/\bullet OH + OH^-$ (0.34 V vs NHE) but not for $OH^-/\bullet OH$ (1.99 V vs NHE) [22]. Meanwhile, the lack of transfer path for carriers to desire sites on pristine CN results in rapid carrier recombination [23]. Recognizing the direct influence of surface structure on band structure and carrier migration, redesigning the surface structure of CN is expected to enable the effective reduction of H_2O_2 by e^- and oxidation of OH^- by h^+ to produce $\bullet OH$ storm for cancer therapy. Moreover, oral squamous cell
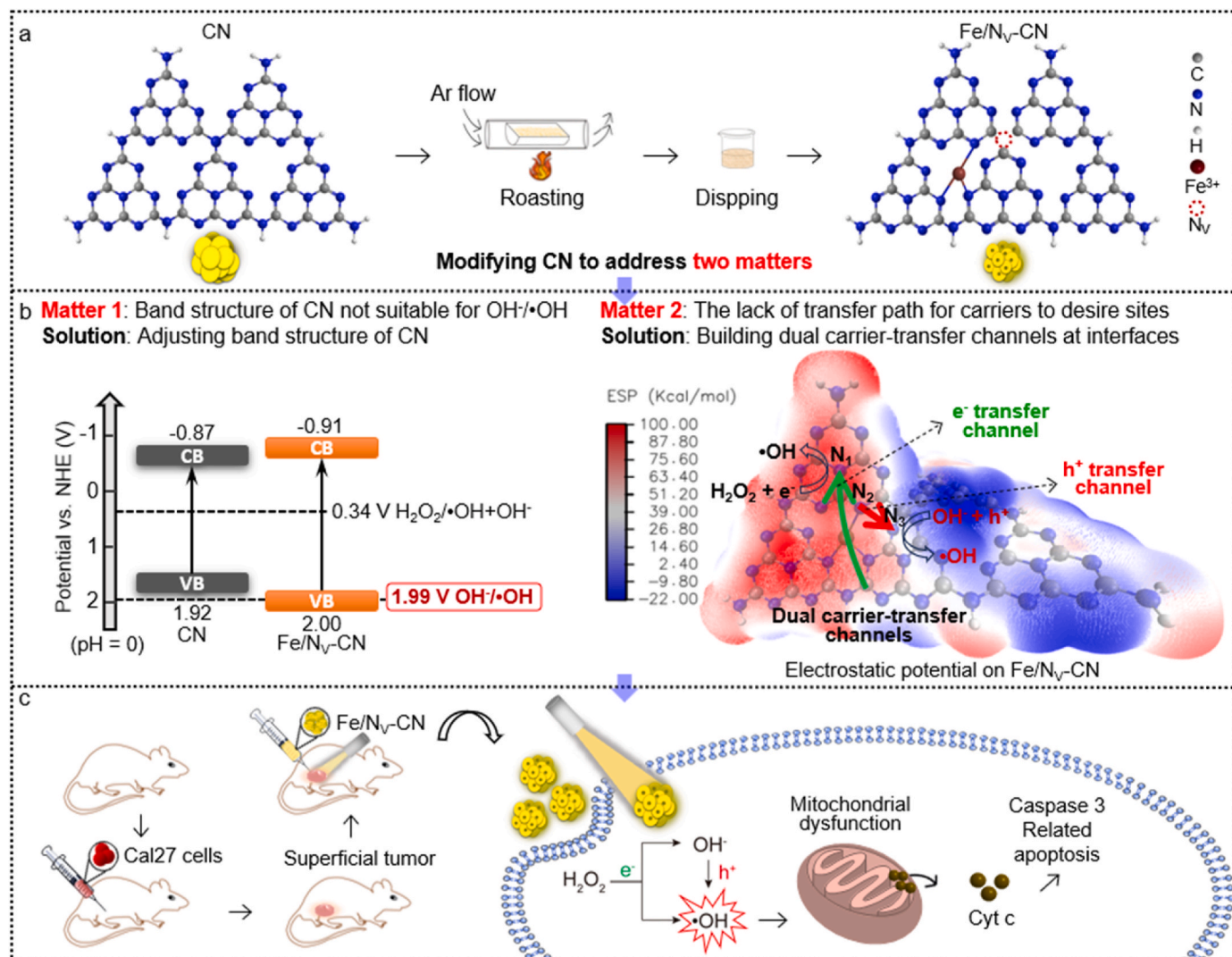
Scheme 1. The antitumor mechanism of Fe/N_V-CN. (a) Synthetic procedure of Fe/N_V-CN. (b) Two matters restricting therapy effect of CN and corresponding solutions. (c) Illustration of therapeutic design and detailed processes of cancer cell apoptosis.

carcinoma (OSCC) is a typical superficial tumor with an overall 5-year survival rate below 60 %, even with multiple treatments. The substantial mutilation associated with current treatment approaches, underscores the need of effective modification strategies for CN, making OSCC an apt model for such studies.

In this study, we designed Fe/N_V-CN, a composite material featuring co-modification with nitrogen vacancies (N_V) and ferric ions (Fe^{3+}) (Scheme 1a). N_V increase the electron density in "nitrogen pots" to promote the rivet of Fe^{3+} (existing as single atoms). N_V and Fe^{3+} synergistically adjust the band structure of CN via quantum confinement effect (induced by the reduced nanosheet size) and the altered coupled oscillations of atomic orbitals, which allows h^+ to oxidize OH^- to •OH. In addition, N_V and Fe^{3+} collaboratively establish dual carrier-transfer channels for e^- and h^+ respectively directing to reduction sites of H_2O_2 and oxidation sites of OH^-. This is achieved by introducing stepped electrostatic potential (ESP) and shortening three-electron bond between N_2–N_3 (Scheme 1b). Vast •OH induced by Fe/N_V-CN under visible light (VIS) triggers Caspase 3 related apoptosis of Cal27 cells. This process involves mitochondrial dysfunction and the release of cytochrome *c* (Cyt *c*) from mitochondria to cytoplasm. Under VIS, Fe/N_V-CN significantly reduces the size of the xenograft tumor model induced by Cal27 cells. This research not only introduces an effective CN-based photosensitizer for cancer therapy, but also offers a novel approach for surface engineering strategies of semiconductor photosensitizers through the successful regulation of band structure and the construction of dual carrier-transfer channels.

2. Experimental and computational details

2.1. Catalyst preparation

2.1.1. Pristine graphite carbon nitride (CN) nanosheet

Roasting melamine (10 g) in a covered crucible (the temperature rose from 25 °C to 550 °C at a constant rate within 210 min and maintained for 4 h). The resulted powder material was treated in rolling HNO_3 (5 M, 100 mL) for 12 h, rinsed with distilled water (ddH_2O) until neutral and then redispersed in ddH_2O (100 mL). The resultant suspension solution was sonicated for 6 h and the remaining unexfoliated sheets was removed by centrifugation (1500 rpm, 5 min). Finally, the obtained material was dried at 60 °C for 12 h.

2.1.2. Nitrogen vacancy modified CN (N_V-CN)

CN (0.3 g) was calcinated in a tube furnace at 520 °C for 1 h under high purity argon gas flow (heating rate of 10 °C·min^{-1}).

2.1.3. Fe^{3+} doped CN (Fe-CN)

Dissolving $Fe(NO_3)_3$·$9H_2O$ (0.025 mg) and CN (0.2 g) in ethanol (15 mL) and stirring at 25 °C for 24 h. Separating the precipitates and washing it three times with ethanol. Then the product was dried at 60 °C for 12 h.

2.1.4. Fe^{3+} and N_V co-modified CN (Fe/N_V-CN)

$Fe(NO_3)_3$·$9H_2O$ (0.025 mg) and N_V-CN (0.2 g) were processed in accordance with the procedure as above.

2.1.5. Cy5.5-labeled Fe/N_V-CN (Cy5.5-Fe/N_V-CN)

Cy5.5 (0.25 mg) and Fe/N_V-CN (25 mg) were dissolved in PBS (5 mL) and stirred for 24 h (25 °C). The solid was rinsed three times with PBS and redispersed into PBS (5 mL).

2.2. Materials characterization

The appearance of samples was revealed via transmission electron microscope (TEM, instrumental model: Tecnai G2 F20 S-Twin). The particle size distribution of samples was measured on Zetasizer Nano ZS-90. The crystal structure of samples was revealed by Bruker D8

Advanced diffractometer (equipping with Cu Kα X-ray source). Both the bonds in samples and the decomposition process of H_2O_2 on samples (adding 10 μL of H_2O_2 into reaction chamber and purging for 10 min before testing) were studied via Bruker Tensor II spectrometer. The maps of C, N and Fe on Fe/N_V-CN were explored by energy-dispersive X-ray spectroscopy (EDX, instrumental model: Talos F200S G2). Fe single atom was characterized by aberration corrected scanning transmission electron microscopy (AC-STEM, Titan Themis 60-300). Inductively coupled plasma (ICP) emission spectroscopy measurement was conducted on Thermo Icap6300 instrument. Testing the specific surface areas of pristine and modified carbon nitride via nitrogen adsorption-desorption measurement on QUADRASPRB evo instrument. Elemental analysis (EA) was proceeded via Vario EL CUNE instrument. Electronic transfer between atoms was explored via X-ray photoelectron spectroscopy (XPS) spectra (instrumental model: AXIS ULTRA DLD). The light absorption capacity of samples was explored via UV–Vis diffuse reflectance (UV–Vis) spectra (instrumental model: HITACHI U-3900). Details of photoelectrochemical measurements were shown in SI. *In-situ* electron paramagnetic resonance (EPR) signals were recorded with white LED light irradiation of 5 min using DMPO as radical scavenger (instrumental model: EMXPLUS10/12). The preparation method of test liquid sample: 225 μg of catalyst, 5 μL of H_2O_2 and 20 mg of 5,5-Dimethyl-1-pyrroline N-Oxide (DMPO) were added in 65 μL of acetonitrile. The degradation reaction of methyl blue (MB) was also evaluated on HITACHI U-3900 spectrometer.

2.3. Computational details

Density functional theory (DFT) calculations were proceeded with the Gaussian 16 program. Optimized catalyst models on account of B3LYP/6-31 g** method. All models were drawn with the Multiwfn and VMD program based on the optimized results.

2.4. Cell culture

Culturing human oral squamous cell carcinoma (Cal27) cells in incubator (Thermo Scientific, 37 °C, filled with 5 % CO_2). Culture medium: DMEM (high glucose, containing sodium pyruvate, 45 mL), FBS (Gibco, 5 mL), penicillin/streptomycin (0.5 mL) and L-glutamine (Meilunbio, 0.5 mL). The digestive process was carried out in trypsin-EDTA solution (Gibco, 0.25 %) and followed by a resuspension process in fresh medium for passage of cell.

2.5. Uptake and intracellular distribution of Fe/N_V-CN

Cal27 cells were cultured in a 24-well plate (1×10^5 cells per well, 24 h), incubated with Fe/N_V-CN (1 mg mL^{-1}, 500 μL, 1, 3, 6 or 9 h), rinsed using PBS, and disposed with paraformaldehyde (4 %, 15 min) and 2-(4-amidinophenyl)-6-indolecarbamidine dihydrochloride (DAPI, 5 μg mL^{-1}, 10 min). The observation process was carried out via confocal laser scanning microscopy (CLSM, Olympus, FV3000).

2.6. Photocatalytic treatment process for cancer cell

Cal27 cells were cultured in a 96-well plate (1.2×10^4 cells per well, 24 h), incubated with Fe/N_V-CN (1 mg mL^{-1}, 100 μL, 6 h), rinsed using PBS, illuminated with white LED light (50 mW cm^{-2}, 30 min, the spectrum of light source was shown in Fig. S1) and then cultured for another 24 h. Analyzing the cells via cell counting kit-8 (CCK-8) and 5-ethinyl-2′-deoxyuridine (EdU) assays according to the specification.

2.7. Intracellular pH indication

BBcellProbe P01 was used to indicate the intracellular pH. Cal27 cells were cultured in a 96-well plate (1.2×10^4 cells per well, 24 h), incubated with CN or Fe/N_V-CN (1 mg mL^{-1}, 100 μL, 6 h), rinsed using

PBS, illuminated with white LED light (50 mW cm^{-2}, 30 min). Then the cells were incubated with the probe dyeing solution made up according to the specification for 1 h, rinsed and re-suspended with PBS. The fluorescein emissions of cells excited by light at wavelengths of 488 nm and 440 nm were measured via fluorescent enzyme labeling instrument (Thermo Scientific, Varioskan LuX).

2.8. Detection of intracellular •OH

Cal27 cells were cultured in a 6-well plate (2.0×10^6 cells per well, 24 h), incubated with Fe/N$_V$-CN (1 mg mL^{-1}, 2 mL, 6 h), rinsed using PBS, co-cultured with HKOH-1r (8 μM, 30 min) and then irradiated with white LED light (50 mW cm^{-2}, 30 min). Finally, the fluorescence intensity was detected using flow cytometry (Agilent Corporation, novocyte).

2.9. Mitochondrial JC-1 staining assay

Cal27 cells were cultured in a 24-well plate (1×10^5 cells per well, 24 h), incubated with Fe/N$_V$-CN (1 mg mL^{-1}, 500 μL, 6h), rinsed using PBS, irradiated with white LED light (50 mW cm^{-2}, 30 min) and cultured for another 24 h. Subsequently, the cells were incubated with JC-1 dyeing solution according to the specification (37 °C, 20 min) and rinsed using JC-1 dye buffer for three times. The corresponding images were presented via CLSM.

2.10. Western blot analysis

Cal27 cells were cultured in a 6-well plate (2×10^6 cells per well, 24 h), incubated with Fe/N$_V$-CN (1 mg mL^{-1}, 2 mL, 6 h), rinsed with PBS, irradiated with white LED light (50 mW cm^{-2}, 30 min) and cultured for 24 h. The extraction and quantification of total protein were severally performed using RIPA lysis buffer and bicinchoninic acid (BCA) protein kit. Proteins were separated and transferred, and the membranes were blocked using protein-free rapid blocking solution (Boster, 25 °C, 20 min) and then incubated with various antibodies (4 °C, 12 h). Membranes were rinsed and disposed with conjugated anti-rabbit IgG antibodies (25 °C, 1 h). The contents of Cyt c in cytoplasm, pro Caspase 3 and cleaved Caspase 3 were examined using the Compass software (Bio-Rad chenidoc XRS+, Universal Hood II).

2.11. Cleaved Caspase 3 immunofluorescent staining

Cal 27 cells were cultured in a 24-well plate (1×10^5 cells per well, 24 h), incubated with Fe/N$_V$-CN (1 mg mL^{-1}, 500 μL, 6 h), rinsed using PBS, irradiated with white LED light (50 mW cm^{-2}, 30 min), fixed by paraformaldehyde (4 %, 25 °C, 15 min), and rinsed again using PBS. The treated cells were disposed with Triton X-100 (0.5 %, 5 min), rinsed again using PBS and incubated with BSA (1 %, 30 min) to lock unspecific sites. Afterwards, the cells were successively co-cultured with cleaved Caspase 3 primary antibody (Cell Signaling, 1:1500 dilution, 4 °C, 12 h) and Alexa Fluor plus Cy5-labeled goat anti-Rabbit IgG (Servicebio, GB27303, 25 °C, 1 h), and then rinsed using PBS. Subsequently, the cells were stained with DAPI (10 min) and washed using PBS. Finally, the cells dispersed in PBS were visualized via CLSM.

2.12. Cell apoptosis assessment by flow cytometry

Annexin V-FITC/PI apoptosis detection kit (Bestbio, BB4126) was used for determining the mode of Cal27 cells death. Cal27 cells were cultured in a 6-well plate (2×10^6 cells per well, 24 h), incubated with Fe/N$_V$-CN (1 mg mL^{-1}, 2 mL, 6 h), irradiated with white LED light (50 mW cm^{-2}, 30 min) and cultured for another 24 h. The treated cells were dyed with Annexin V-FITC/PI apoptosis detection kit according to the specification for flow cytometry.

2.13. Antitumor efficacy assay in vivo

All experiments of animal were strictly carried out under the ethical regulations permitted by the Animal Ethics Committee of the Second Hospital of Shanxi Medical University (DW2023049). The female BALB/c mice (3–4 weeks) were randomly assigned and kept in standard conditions. The mice were injected subcutaneously with Cal27 cells (2×10^7 cells per mice) in right hind legs side axilla and then divided into different groups after tumor grew to 100 mm^3 (PBS, PBS + Light, Fe/N$_V$-CN, and Fe/N$_V$-CN + Light groups, six mice in each group). The mice were injected intratumorally with 50 μL of PBS or Fe/N$_V$-CN (1 mg mL^{-1}). Illumination (white LED light, 50 mW cm^{-2}, 30 min) was administered after 6 h. Drug administration and illumination were performed every two days for a total of 4 times. The body weight and tumor volume (long diameter × short diameter × short diameter × 0.5) were measured every two days. On day 22, the blood of mice was collected for hematology analysis and blood biochemistry analysis [liver (AST, ALT) and kidney (CRE, Urea) function indexes]. Then, all the mice were sacrificed and the subcutaneous tumors were isolated and weighted. Moreover, the isolated tumors and major organs were obtained for histopathological examination.

2.14. Biodistribution and tumor accumulation of Fe/N$_V$-CN

Cal27 tumor-bearing mice were intratumorally injected with Cy5.5-labeled Fe/N$_V$-CN (5 mg mL^{-1}, 50 μL) after the tumor growing to 150–200 mm^3 and the fluorescence was observed using IVIS at 0.5, 1, 3, 6, 9, 12, 24, 48 and 72 h after injection. Mice were sacrifieced and the major organs (heart, liver, spleen, lung and kidney) and tumors were retained for *ex vivo* imaging at different time points.

2.15. In vitro biocompatibility

The blood of mice was collected and centrifuged to obtain blood cells precipitation. Then the blood cells (RBC) were respectively mixed with PBS solutions containing different concentrations of Fe/N$_V$-CN at 25 °C for 4 h. Using PBS and ddH$_2$O for the negative and positive control group, severally. The images were acquired after centrifugal treatment (3000 rpm, 15 min) and the absorbance of supernatants at the wavelength of 540 nm in various groups were detected. Hemolysis rate (%) = (OD$_X$ - OD$_{negative}$)/(OD$_{positive}$ - OD$_{negative}$) × 100 %.

2.16. Histopathological examination

The slices of organs and tumors were proceeded with hematoxylin and eosin (H&E) staining and observed using light microscopy. The slices of tumor were also tinted with terminal deoxynucleotidyl transferase dUTP nick end labeling (TUNEL) and cleaved Caspase 3 antibody, and obtained immunofluorescence images via inverted luminescence microscope.

2.17. Statistical analysis

Data were shown as mean ± standard deviation (SD). The statistical analyses and graphing were performed by GraphPad Prism. Using student's *t*-test and one-way analysis of variance for data comparison. *, ** and ***, severally corresponding $p < 0.05$, <0.01 and <0.001, represent statistically significant data.

3. Results and discussion

3.1. Structural characterization of modified CN samples

Both transmission electron microscopy (TEM) images of Fe/N$_V$-CN and N$_V$-CN displayed flake morphologies with size about 100 nm, smaller than that of Fe-CN and CN (about 200 nm) (Fig. 1a and S2),
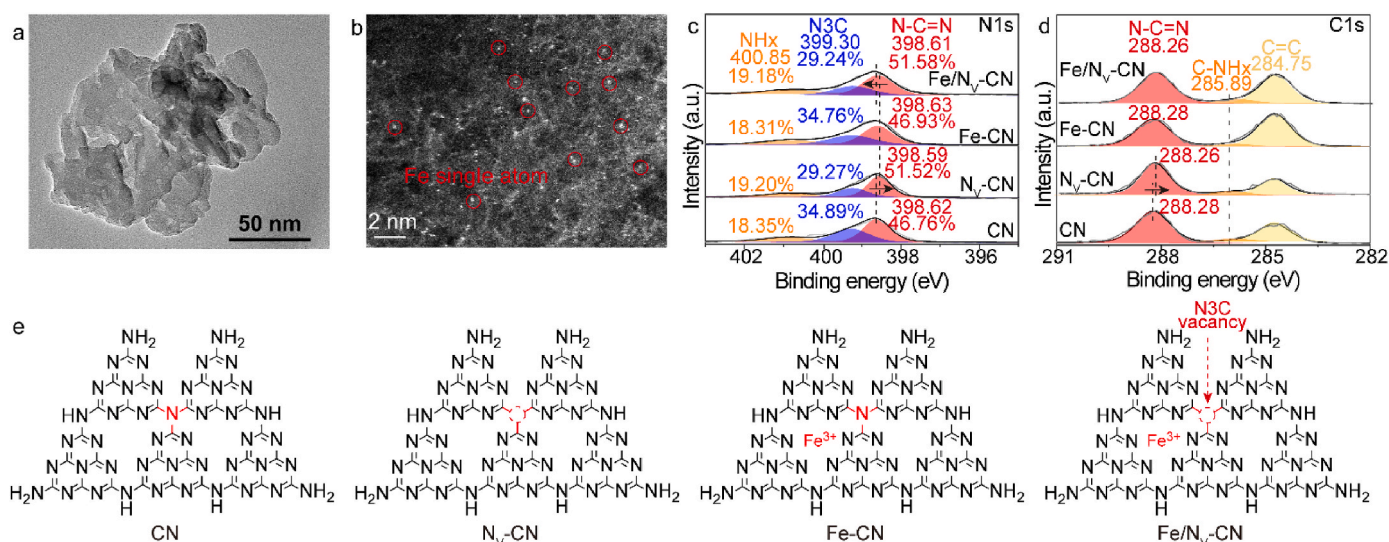
Fig. 1. Structural characterization of samples. (a) TEM image and (b) AC-STEM image of Fe/N_V-CN. XPS spectra of (c) N1s and (d) C1s in pristine and modified carbon nitride. (e) Schematic structures of pristine and modified carbon nitride.

which is consistent with the results of dynamic light scattering (DLS) (Fig. S3). The chemical structures of samples were studied by powder X-ray diffraction (XRD) patterns and Fourier transform infrared (FTIR) spectra. As shown in Figs. S4 and S5, the similar XRD patterns and FTIR spectra for all samples indicate that the general structure of carbon nitride was preserved after introducing vacancies and ferric ions (Fe^{3+}). CN shows two characteristic peaks around 13.3° and 27.5° (Fig. S4), indexed to in-plane s-heptazine units and conjugated melon structures along (100) and (002) planes, respectively [24]. The slightly weaker peaks in Fe/N_V-CN and N_V-CN than Fe-CN and CN, respectively, suggesting the destructed crystalline structures after introducing vacancies, consistent with the results of TEM (Fig. 1a and S2). The peaks in FTIR spectra around 3500-3000, 1800-1100 and 810 cm^{-1} correspond to N–H and O–H stretching vibration, N–C=N stretching vibration and breathing mode of triazine rings, respectively (Fig. S5) [25]. The N–C=N stretching vibration in Fe/N_V-CN and Fe-CN gets weaker than in N_V-CN and CN, which suggests the interaction between Fe^{3+} and N of "nitrogen pot" in Fe/N_V-CN and Fe-CN [26]. *In-situ* DRIFT spectrum of Fe/N_V-CN with N_V-CN as background was used to study the bond between Fe^{3+} and carbon nitride. As shown in Fig. S6, the peaks around 1850-1300 cm^{-1} and 725 cm-1, assign to N–C=N and Fe–N stretching vibration, respectively, which verifies the formation of coordination bond between Fe^{3+} and N in "nitrogen pot" [27].

The energy-dispersive X-ray spectroscopy (EDX) confirms that C, N and Fe elements uniformly distribute on Fe/N_V-CN (Fig. S7). Aberration corrected scanning transmission electron microscopy (AC-STEM), with extremely high resolution, was used to prove the existence of Fe^{3+} in the form of signle atoms. The bright dots sparking on Fe/N_V-CN attribute to Fe single atoms due to the higher electron density of Fe than C and N (Fig. 1b) [28]. The contents of Fe^{3+} in Fe/N_V-CN and Fe-CN were detected using inductively coupled plasma (ICP, Table S1). The more Fe^{3+} in Fe/N_V-CN (8.85 ppm) than in Fe-CN (3.30 ppm), may attributes to the bigger specific surface area of N_V-CN (32.0 m^2 g^{-1}) than CN (25.1 m^2 g^{-1}) (Table S2) and the stronger interaction between Fe^{3+} and N_V-CN than CN [29]. In general, Fe^{3+} uniformly distributed on Fe/N_V-CN in the form of single atoms and the secondary roasting of carbon nitride benefits the loading of Fe^{3+}, which is discussed in detail in the following section.

The type of vacancy was characterized by elemental analysis (EA) and X-ray photoelecctron spectroscopy (XPS) (Table S3). The higher C/N (at.%) in N_V-CN (63.92 % and 71.66 %) than CN (63.76 % and 71.00 %) severally measured by EA and XPS, indicates the successful

introduction of nitrogen vacancies (N_V). The larger difference in C/N (at. %) between CN and N_V-CN measured by XPS than EA shows that N_V distributes on the outer layer of N_V-CN. The more stronger electron paramagnetic resonance (EPR) signals of N_V-CN with g-value of 2.005 than CN, also attributes to the introduction of N_V (Fig. S8) [30].

The peaks around 400.85, 399.30 and 398.61 eV, assign to N species in NH$_X$, N3C and N–C=N in Fe/N_V-CN, respectively (Fig. 1c) [31]. The peak-area ratio of N3C decreases from 34.89 % in CN to 29.27 % in N_V-CN. Combining with the consistent breathing vibration peak of triazines in CN and N_V-CN (Fig. S5), it was concluded that N3C connecting three heptazines was bombarded during secondary calcination. The peaks at 288.26, 285.89 and 284.75 eV, assign to C species in N–C=N, C–NH$_X$ and adventitious C=C bonds (Fig. 1d) [32]. The shifts to lower bending energy of N1s and C1s peaks of N–C=N after introducing N_V, attributes to the electron enrichment around N_V, makeing N_V ideal reactive sites [32]. The more obviously shift to higher bending energy of N1s peak of N–C=N between Fe/N_V-CN (398.61 eV) and N_V-CN (398.59 eV) than Fe-CN (398.63 eV) and CN (398.62 eV), shows the more electron transfer from N to Fe^{3+} in Fe/N_V-CN than Fe-CN, which indicates the stronger interaction between Fe^{3+} and N in Fe/N_V-CN than Fe-CN, consistent with the results of ICP (Table S1) [33]. The feeble Fe2p signal in Fig. S9 attributes to the trace amounts of Fe^{3+} in Fe/N_V-CN, consistent with the results of ICP (Table S1). According to above analysis, it was concluded that N3C vacancies were introduced into carbon nitride after secondary calcination and Fe^{3+} were loaded in "nitrogen pots" of Fe/N_V-CN as single atoms (Fig. 1e) accompanying with electron transfer from N to Fe^{3+}.

3.2. Analysis of band structures and dual carrier-transfer channels

The band structures of samples were explored via UV–Vis spectra and Mott-Schottky (MS) curves. The bandgap (E_g) of Fe/N_V-CN (2.91 eV) is larger than Fe-CN (2.81 eV), N_V-CN (2.85 eV) and CN (2.79 eV) by fitting Tauc plots (Fig. 2a), assigning to the quantum confinement effect (QCE, induced by the reduced nanosheet size after introducing N_V) and the altered coupled oscillations of atomic orbitals.

(induced by the introdution of N_V and Fe^{3+}) [22]. N_V-CN, Fe-CN and Fe/N_V-CN show slightly greater light absorption capacities than CN in the wavelength range of 480–780 nm (Fig. S10), assigned to the midgap states caused by N_V or Fe^{3+} [34]. All samples are *n*-type semiconductors according to MS curves (Fig. 2b), the values of flat band potentials of CN, N_V-CN, Fe-CN and Fe/N_V-CN severally are −1.07, −1.12, −1.04 and
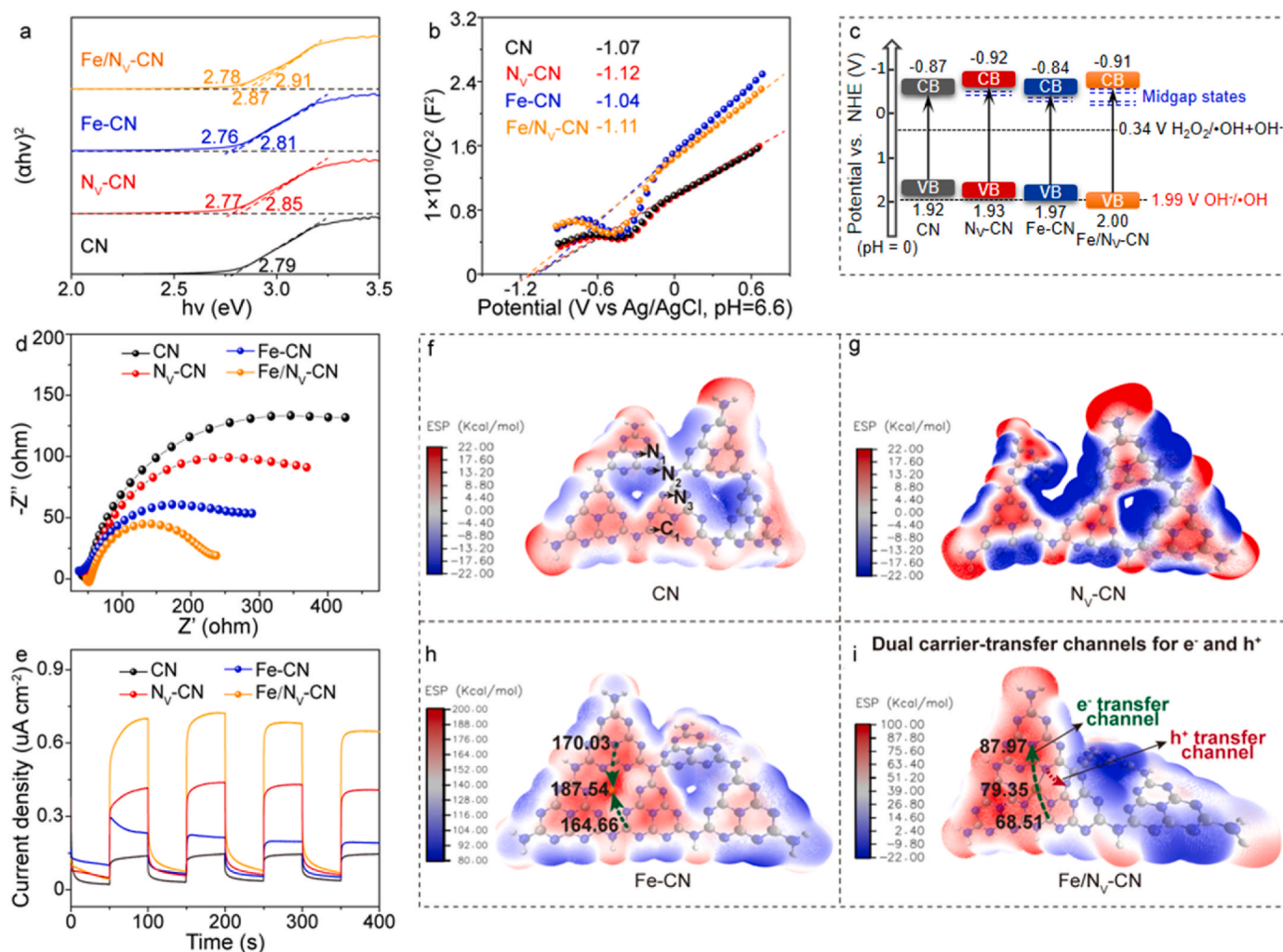
Fig. 2. Band structures and dual carrier-transfer channels characterization. (a) Bandgap energy, (b) Mott-Schottky plots, (c) band structures, (d) EIS Nyquist plots and (e) periodic ON/OFF photocurrent curves under white LED light of pristine and modified CN. The calculated surface electrostatic potential of (f) CN, (g) N_V-CN, (h) Fe-CN and (i) Fe/N_V-CN cluster models.

−1.11 V vs. Ag/AgCl, corresponding to conduction bands (CB) at −0.87, −0.92, −0.84 and −0.91 V vs. NHE (Table S4). The valence bands (VB) of CN, N_V-CN, Fe-CN and Fe/N_V-CN are 1.92, 1.93, 1.97 and 2.00 V vs. NHE calculated combining E_g and CB. Hence, pristine and modified carbon nitride could catalyze the reaction of H_2O_2/•OH + OH^- (0.34 V vs. NHE), while, Fe/N_V-CN could also catalyze the reaction of OH^-/•OH (1.99 V vs. NHE) (Fig. 2c).

The charge transfer kinetics was studied by electrochemical impedance spectroscopy (EIS) and photocurrent response [30]. N_V-CN and Fe-CN show smaller semicircle radii than CN (Fig. 2d), showing both N_V and Fe^{3+} benifit charge transfer. The semicircle radii of Fe/N_V-CN is obviously smaller than Fe-CN and N_V-CN, indicates the synergistic effect of Fe^{3+} and N_V on charge transfer. The stronger photocurrent of Fe/N_V-CN than CN, N_V-CN and Fe-CN (Fig. 2e), attributes to the higher charge transfer kinetics on Fe/N_V-CN, indicating that more carriers on Fe/N_V-CN may be able to participate in surface reaction.

Using density functional theory (DFT) calculation to study the surface electrostatic potential (ESP) based on the cluster models of samples (Fig. S11). Blue and red color severally represent negative and positive ESP. The more negative ESP of "nitrogen pot" attached to N_V in N_V-CN than in CN (Fig. 2f–g), assigning to the electrons redistribution from N_V to adjacent atoms across delocalized π conjugated networks [35], shows that N_V can promote the adsorption of "nitrogen pot" for metal ion. The color of "nitrogen pot" containing Fe^{3+} in Fe-CN turns red (Fig. 2h),

meaning reduced electron migration resistance through this "nitrogen pot". The ESP increases in the order of Fe^{3+} > N_1 > C_1 in Fe-CN (187.54 > 170.03 > 164.66 kcal/mol), showing that Fe^{3+} is a better trapping site of e^- than N_1 and C_1 in Fe-CN [36]. No Fe–N bond appears in Fe-CN but three in Fe/N_V-CN (Fig. 2h–i), indicates the stronger interaction between Fe^{3+} and N_V-CN than CN due to the more negative ESP of "nitrogen pot" in N_V-CN than CN [37]. ESP gradiently distributes on N_1, Fe^{3+} and C_1 in Fe/N_V-CN (87.97 > 79.35 > 68.51 kcal/mol), suggesting that Fe^{3+} in Fe/N_V-CN can act as channel for rapidly transfer of e^- from C_1 to N_1 [34]. The significant lower values of ESP on Fe/N_V-CN than Fe-CN, attribute to the reduced interaction energy between the system and a unit positive point charge at one point due to the electron enrichment after introducing N_V [35,38]. Moreover, as the transfer channel of h^+, three-electron bond (N_2–N_3) distance, directly affects h^+ transfer between heptazines [39]. The shorter N_2–N_3 distance in Fe/N_V-CN (2.442 Å) than in CN (2.801 Å), N_V-CN (5.812 Å) and Fe-CN (2.504 Å) (Table S5), assigning to the formation of coordination bonds between Fe^{3+} and N in Fe/N_V-CN, shows that N_V and Fe^{3+} could promote the transfer of h^+ through N_2–N_3 channel.

Moreover, other N_V and metal ions co-modified carbon nitride, including Co/N_V-CN, Ni/N_V-CN and Cu/N_V-CN, were also synthesised using the same preparation method of Fe/N_V-CN. The introduction of Fe^{3+}, Co^{2+} and Ni^{2+} could further promote the inactivation of cancer cells via constructing dual carrier-transfer channels while Cu^{2+} cannot

(Fig. S12). Therefore, even though the "nitrogen pot" has the potential to adsorb a variety of metal ions, not all metal ions can cooperate with N_V to construct dual carrier-transfer channels. In summary, N_V and Fe^{3+} jointly introduce dual carrier-transfer channels into Fe/N_V-CN for e^- and h^+, speeding up carrier migration and allowing more carriers to participate in the production of •OH.

3.3. Exploration for •OH production pathway

The photocatalytic production of •OH was also explored via electron paramagnetic resonance (EPR) spectra. All sample shows weak signals in the dark (Fig. S13). Under irradiation, Fe/N_V-CN exhibits obviously stronger •OH signals (Fe/N_V-CN + Light) than Fe-CN (Fe-CN + Light), N_V-CN (N_V-CN + Light) and CN (CN + Light) (Fig. 3a), displaying more efficient generation of •OH over Fe/N_V-CN than others [34]. •OH could degrade methylene blue (MB) to colourless products, and there is a linear relationship between concentrations and maximum absorbances in UV–Vis spectra of MB (Figs. S14a–b) [40]. Photodegradation reaction of MB was used to further verify the •OH generation ability of various carbon nitride and the production pathway of •OH over Fe/N_V-CN. With the molecular ration of MB and H_2O_2 of 2:1 in argon atmosphere (Ar, 1 atm), the maximum degradation rate of MB can only reach 50 % if reduction of H_2O_2 is the only way to produce •OH. Under illumination, the obviously higher reaction rate over Fe/N_V-CN (81.1 %) than CN (15.7 %), N_V-CN (39.1 %) and Fe-CN (40.2 %) (Fig. 3b and S14c-d), not only indicates the synergistic effect of N_V and Fe^{3+} in •OH production, but also indicates the presence of pathway to produce •OH by oxidizing OH^- (the inset in Fig. 3b).

The production path of •OH was aslo revealed by *in-situ* DRIFT spectra (Fig. 3c and S15). The band at 855 cm^{-1}, HO–OH stretching vibration [41], shows stronger intensity in Fe/N_V-CN and N_V-CN than Fe-CN and CN, indicating that N_V promote the adsorption of H_2O_2 by increasing the electron density of triazine ring. HO–OH stretching vibration peak in Fe/N_V-CN, gets weaker and shifts to higher wavenumber with the prolonged illumination time. The bands at 1592 (N–C=N stretching vibration of carbon nitride) and 1363 cm^{-1} (CN–O stretching vibration between H_2O_2 and carbon nitride), weaken faster with the extended irradiation time in Fe/N_V-CN than in others. It indicates that the adsorbed H_2O_2 on Fe/N_V-CN quickly reduces to •OH and OH^- benefiting from the dual carrier-transfer channels [34,42]. The band at
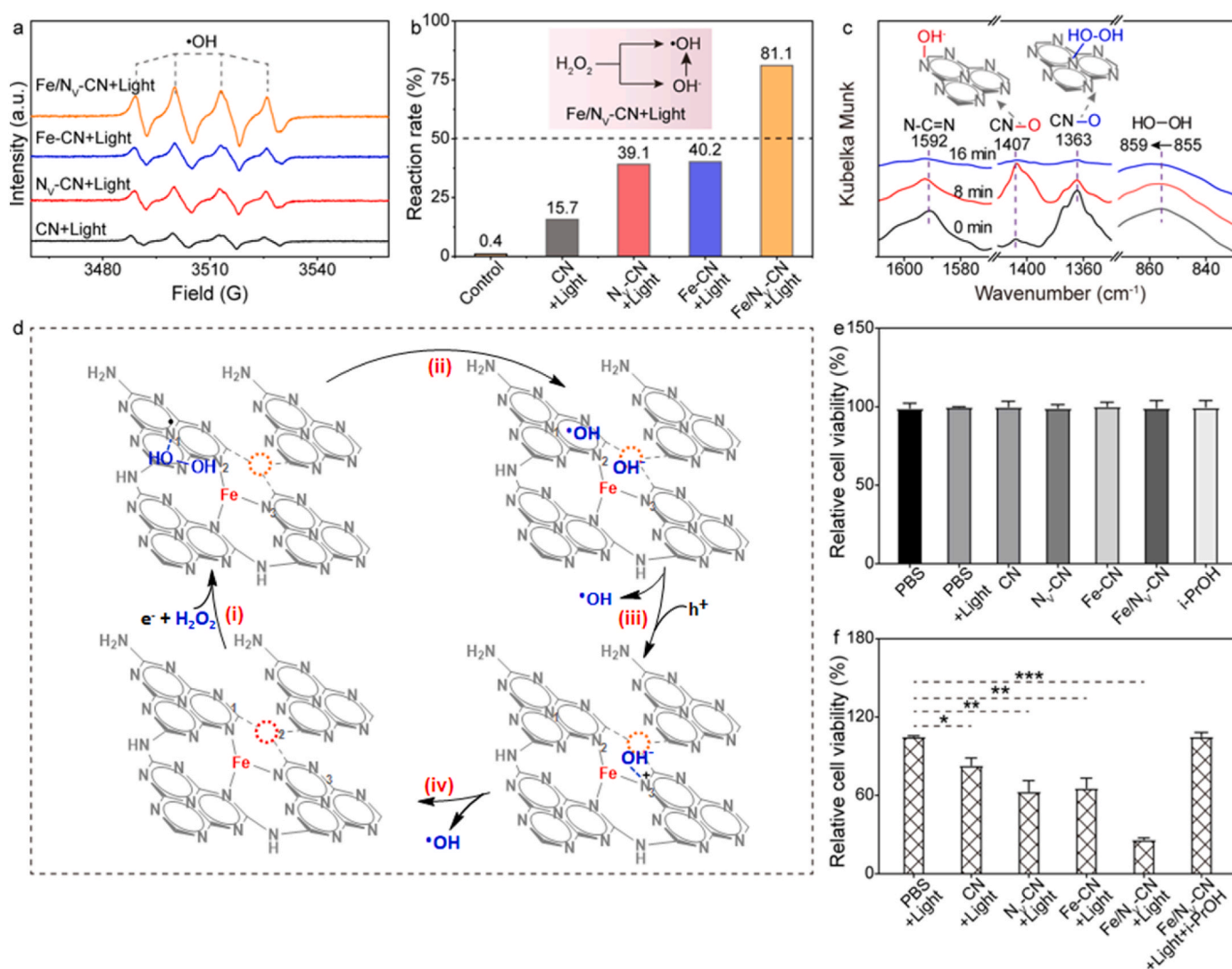
Fig. 3. Exploration of •OH formation path. (a) *In-situ* EPR spectra. (b) Photocatalytic degradation of MB. Reaction conditions: MB solution (5 mL, 10 mg L^{-1}); the molecular ration of MB and H_2O_2 is 2:1; catalyst (5 mg); Ar (1 atm); 30 °C; 20 min; white LED light (300 mW cm^{-2}). (c) Time course *in-situ* DRIFT spectra of H_2O_2 on Fe/N_V-CN under white LED light. (d) Proposed mechanisms for photocatalytic H_2O_2 reduction on Fe/N_V-CN. (e) Influences evaluation of white LED light, CN, N_V-CN, Fe-CN, Fe/N_V-CN or i-PrOH on Cal27 cells by CCK-8 assay. (f) Cell viability assay of Cal27 cells treated with PBS, CN, N_V-CN, Fe-CN, Fe/N_V-CN and Fe/N_V-CN + i-PrOH under white LED light.

1407 cm^{-1}, CN–O stretching vibration between OH$^-$ and carbon nitride, strengthens at 8 min mark in all four samples while then weakens at 16 min mark only in Fe/N$_V$-CN, indicating that OH$^-$ can oxidized to •OH by h$^+$ only in Fe/N$_V$-CN system [43]. Hence, we infer about the generation process of •OH over Fe/N$_V$-CN (Fig. 3d). (i) H$_2$O$_2$ is adsorbed on N$_1$ site via CN–O bond and (ii) reduced to •OH and OH$^-$ by e$^-$; (iii) h$^+$ oxidates OH$^-$ adsorbed on N$_3$ site and (iv) produces another •OH.

Combining with the results of band structure characterization, EIS, photocurrent response and DFT calculation, we definitely propose that the co-modification of N$_V$ and Fe^{3+} not only adjust the band structure of carbon nitride to allow Fe/N$_V$-CN to reduce H$_2$O$_2$ to •OH and OH$^-$, meanwhile oxidize OH$^-$ to •OH, but also induce dual carrier-transfer channels for e$^-$ and h$^+$ severally directing to H$_2$O$_2$ reduction site and OH$^-$ oxidization site, which leads to the rapid formation of vast •OH over Fe/N$_V$-CN.

3.4. Investigation of Fe/N$_V$-CN PDT efficacy in vitro

PDT efficacy of Fe/N$_V$-CN and the necessity of •OH for killing Cal27 cells were accessed by measuring cell viability [44]. 50 mW cm^{-2}, the

maximum light intensity with little effect on cell survival, was selected for subsequent PDT therapy (Fig. S16). The decrease in cell viability at high light intensity may be attributed to the thermal damage of cells caused by the red light (610–730 nm) component in white LED light (Fig. S1). Under white LED light (50 mW cm^{-2}), the ratio of dark to light toxicity (phototoxic index, PI) of Fe/N$_V$-CN is about 26 (Fig. S17). And based on the concentration-dependent curve on PDT of Fe/N$_V$-CN (Fig. S17b), 1 mg mL^{-1} was chosen as the concentration parameter of photosensitizer for cancer cell inactivation. No noticeable adverse effects appeared on cells after incubating with CN, N$_V$-CN, Fe-CN, Fe/N$_V$-CN or isopropyl alcohol (i-PrOH, the volume ratio of i-PrOH to medium was 1:100) (Fig. 3e), showing the little effect of pristine and modified CN or i-PrOH on Cal27 cells. The little hemolysis caused by Fe/N$_V$-CN at various concentrations also proves the good biocompatibility of Fe/N$_V$-CN (Fig. S18). Fe/N$_V$-CN displayed obviously more efficient cell ablation ability than CN, N$_V$-CN and Fe-CN under irradiation (cell viability severally at about 25 %, 79 %, 61 % and 64 %), indicating the synergistic effect of N$_V$ and Fe^{3+} on photocatalytic ablation of Cal27 cells (Fig. 3f). In addition, the obviously lower ratio of red and blue fluorescence area with EdU assay for Fe/N$_V$-CN + Light group
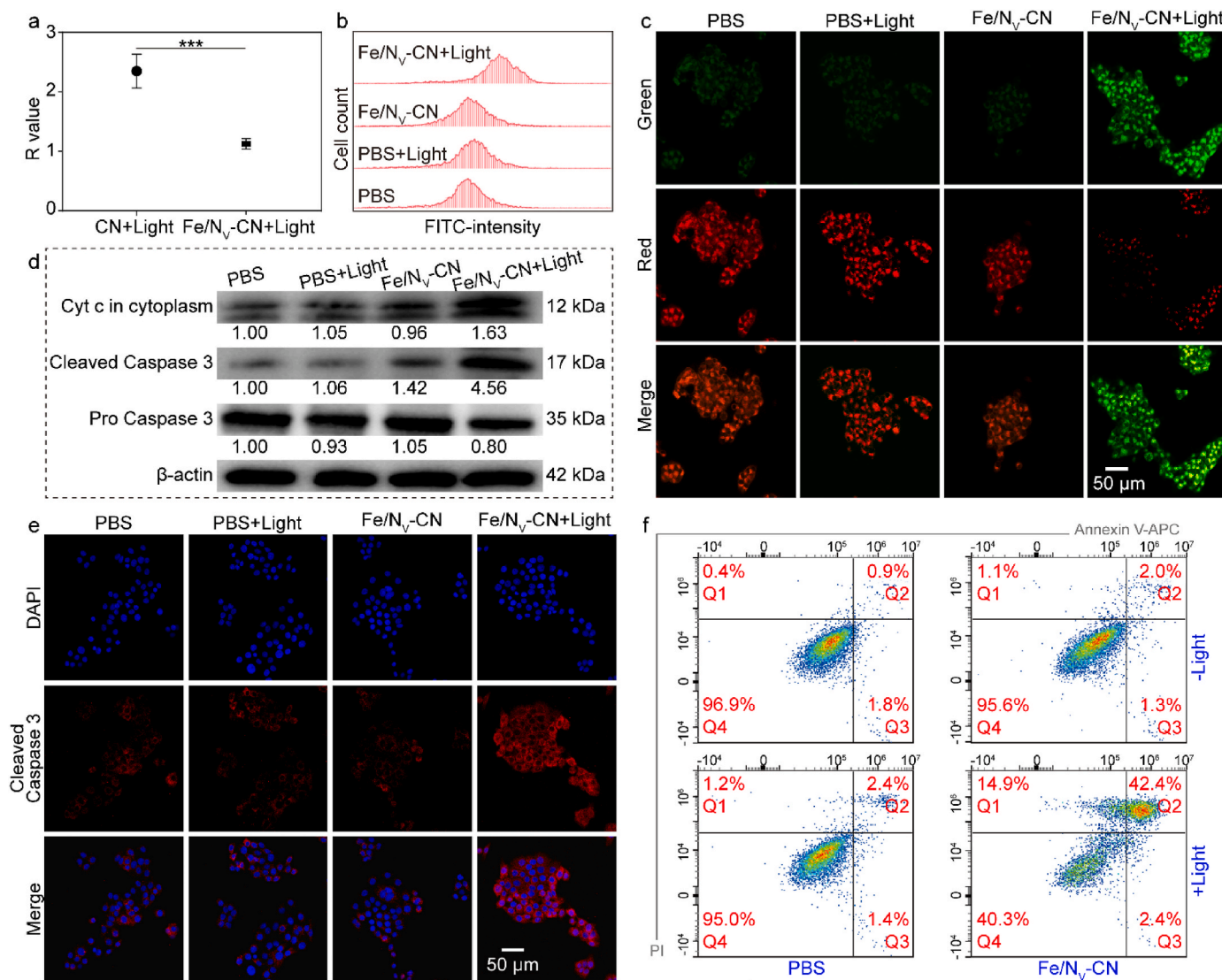
Fig. 4. Study on the mechanism of Cal27 cell apoptosis. (a) R values of Cal27 cells after treated with CN plus light or Fe/N$_V$-CN plus light. (b) Detection of •OH in Cal27 cells in various groups via flow cytometry. (c) CLSM images of Δψm alterations of Cal27 cells in various groups. (d) Western blot analysis of Cyt *c* in cytoplasm, pro Caspase 3 and cleaved Caspase 3 in various groups. (e) CLSM images of cleaved Caspase 3 in Cal27 cells of various groups. (f) Apoptosis flow cytometry results with Annexin V-FITC/PI staining on Cal27 cells.

than PBS, PBS + Light and Fe/N$_V$-CN groups, corroborates the results of CCK-8 assay (Figs. S19–20). However, photocatalytic inactivation effect for Cal27 cells of Fe/N$_V$-CN disappeared after adding i-PrOH (scavenger of •OH) into the medium, indicating that •OH is the main active specie among various ROS in this system for killing Cal27 cells (Fig. 3f) [45]. Therefore, Fe/N$_V$-CN exhibited better photocatalytic inactivation effect for Cal27 cells than pristine and mono-modified CN relying on the vast •OH produced on Fe/N$_V$-CN under light.

3.5. Exploration for Cal27 cells inactivation mechanism

Excellent cell uptake of photosensitizer is required for PDT. The cellular uptake of Fe/N$_V$-CN was evaluated by confocal laser scanning microscopy (CLSM) utilizing its luminescence [2]. With the extension of incubating time, Fe/N$_V$-CN (green fluorenscence) was clearly observed around cell necleus (blue fluorenscence) while rarely in necleus (Fig. S21), showing that Fe/N$_V$-CN was internalized into Cal27 cells and localised in cytoplasm.

The intracellular pH of Cal27 cells after different treatments was tested via fluorescent enzyme labeling instrument to further verify the oxidization of OH$^-$ to •OH in cells. The fluorescein emission ratio (R value) of cells excited by light at wavelengths of 488 nm (F488) to 440 nm (F440), is linearly positively correlated to pH value [46]. The lower R value of Fe/N$_V$-CN + Light group (about 1.1) than CN + Light group (about 2.4), indicates the less accumulation of OH$^-$ in Fe/N$_V$-CN system, which further confirms the oxidization of OH$^-$ to •OH over Fe/N$_V$-CN (Fig. 4a). Moreover, HKOH-1r was used as the probe to detect intracellular •OH via flow cytometry [47]. The peak of Fe/N$_V$-CN + Light group shifts to higher FITC intensity than others (Fig. 4b), indicating that more intense •OH storm in Fe/N$_V$-CN plus light treated Cal27 cells. Mitochondria is the main target organelle of ROS in cells. Vast intracellular •OH will cause mitochondrial dysfuncytion via destroying proteins or respiratory enzymes of mitochondria [48]. The changes in mitochondrial membrane potential ($\Delta\psi m$) were investigated using JC-1 to indicate mitochondrial dysfunction. The obviously decreased $\Delta\psi m$ in Fe/N$_V$-CN + Light group than others indicates mitochondrial
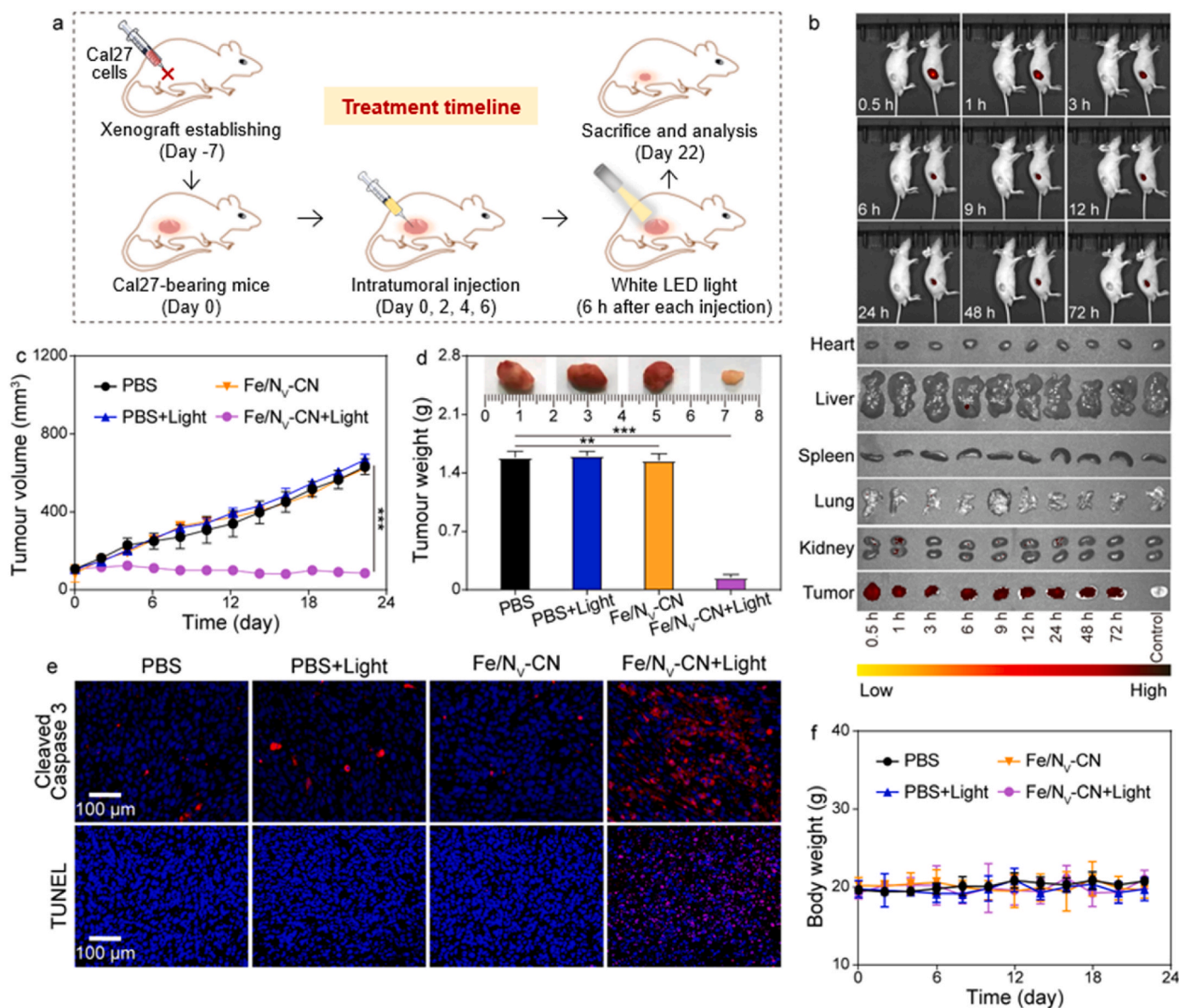
Fig. 5. In vivo anti-tumor effect of Fe/N$_V$-CN mediated PDT. (a) The establishment of tumor xenograft and the strategy of anti-tumor treatment. (b) Fluorescence images of Cal27 tumor-bearing mice after introtumor injection of Cy5.5-labeled Fe/N$_V$-CN and ex vivo fluorescence images of major organs and tumors. (c) Tumor growth curves. (d) The weights and photos of isolated tumors. (e) Cleaved Caspase 3 and TUNEL stained images of tumor slices obtained from tumor-bearing mice in different groups. (f) Body weight curves of mice.

dysfunction of Cal27 cells treated with Fe/N$_V$-CN plus light (Fig. 4c–S22).

The improved membrane permeability caused by mitochondrial dysfunction leads to the exudation of pro-apoptotic factors into cytoplasm, such as cytochrome *c* (Cyt *c*), resulting in the cleavage of Caspase 3 zymogen into subunits and related cell apoptosis [44]. To understand the mechanism of apoptosis triggered by Fe/N$_V$-CN, the contents of Cyt *c* in cytoplasm, pro Caspase 3 and cleaved Caspase 3 were analyzed by western blotting (WB). Fe/N$_V$-CN + light treatment promoted the accumulations of Cyt *c* in cytoplasm and cleaved Caspase 3 while reduce the accumulation of pro Caspase 3 (Fig. 4d). Meanwhile, the strongest immunofluorescence signal of cleaved Caspase 3 was also found in Fe/N$_V$-CN + Light treated Cal27 cells than others (Fig. 4e–S23). Flow cytometry was also performed to determined the apoptosis of Cal27 cells. The significantly increased proportion of cells in Q1-3 regions in Fe/N$_V$-CN + Light group (59.7 %) than in PBS (3.1 %), Fe/N$_V$-CN (4.4 %) and PBS + Light (5.0 %) groups, indicates that Fe/N$_V$-CN can effectually induce apoptosis of Cal27 cells under illumination (Fig. 4f). Therefore, vast ●OH over Fe/N$_V$-CN under illumination leads to mitochondrial dysfunction of Cal27 cells, resulting in the release of Cyt *c* from mitochondrial to cytoplasm and subsequent Caspase 3 related cell apoptosis.

3.6. In vivo studies on tumor treatment

Based on the above results, it was affirmed that the vast ●OH on Fe/N$_V$-CN under illumination can rapidly kill Cal27 cells. Cal27 cells were injected into nude mice to establish tumor-bearing models for evaluating the antitumor therapeutic effect of Fe/N$_V$-CN in vivo (Fig. 5a). Photocatalytic inactivation effect for Cal27 cells depends on the concentration of Fe/N$_V$-CN (Fig. S17b). In order to ensure a relatively high concentration of Fe/N$_V$-CN in tumor during PDT, intratumoral injection was chosen in our animal experiments. Cy5.5-labeled Fe/N$_V$-CN (Fig. S24) was intratumor injected for in vivo imaging to monitor the distribution of Fe/N$_V$-CN (Fig. 5b). The mice were sacrificed and the major organs and tumors were also imaged at different points in time. With 72 h of injection, Fe/N$_V$-CN mainly presented in tumor and some in kigney and liver (Fig. S25), showing that Fe/N$_V$-CN was mainly retained in tumor and some metabolized by kigney and liver. The retention of Fe/N$_V$-CN in tumor attributes to the increased *in-situ* drug bioavailability by intratumoral administration and the impaired lymphatic function in tumor [49,50]. Tumor-bearing mice were randomly divided into PBS, PBS + Light, Fe/N$_V$-CN and Fe/N$_V$-CN + Light groups. These mice were injected with PBS or Fe/N$_V$-CN on day 0, 2, 4 and 6, and additional irradiation was proceeded after 6h of each injection for PBS + Light and Fe/N$_V$-CN + Light groups. Tumor volumes and body weights of mize were monitored every two days and the mice were sacrificed on day 22 to measure tumor mass. On the 22nd day, the tumor volume and weights in PBS, Fe/N$_V$-CN and PBS + Light groups shows little otherness, while Fe/N$_V$-CN + Light group displays significant inhibition of tumor growth, assigning to the apoptosis of Cal27 cells induced by Fe/N$_V$-CN (Fig. 5c–d).

Moreover, the therapeutic effects were investigated by evaluating the histological damages and apoptosis levels of those tumor slices through the hematoxylin and eosin (H&E), cleaved.

Caspase 3 and terminal deoxynucleotidyl transferase dUTP nick end labeling (TUNEL) staining assay, respectively. The most severe histological damages (Fig. S26), strongest expression of cleave Caspase 3 and most obvious apoptosis of tumor tissue were observed in Fe/N$_V$-CN + Light group (Fig. 5e). Although there existed difference in therapeutic efficacy, the average body weights during various treatments showed negligible variation (Fig. 5f). The H&E examinations of major organs (heart, liver, spleen, lung and kidney) were also collected and no significant differences in histological morphology of the major organs were observed in all groups (Fig. S27). Furthermore, blood routine and blood biochemical results did not differ significantly between various groups

(Figs. S28–29). These results validates that Fe/N$_V$-CN possesses good biocompatibility in vivo and is a powerful photosensitizer for photodynamic therapy of cancer.

4. Conclusions

In summary, Fe/N$_V$-CN, co-modified carbon nitride with nitrogen vacancies (N$_V$) and ferric ions (Fe^{3+}), was designed for PDT of oral squamous cell carcinoma. N$_V$ and Fe^{3+} synergistically adjust the band structure of carbon nitride by quantum confinement effect (induced by the reduced nanosheet size) and the altered coupled oscillations of atomic orbitals, allowing Fe/N$_V$-CN to oxidize OH$^-$ to ●OH, which solves the insufficient H$_2$O$_2$ in tumor and the accumulation of OH$^-$ at the same time. Meanwhile, N$_V$ and Fe^{3+} construct dual carrier-transfer channels respectively for e$^-$ to H$_2$O$_2$ reduction site and h$^+$ to OH$^-$ oxidation site, by introducing stepped electrostatic potential (ESP) and shortening three-electron bond. Under illumination, vast ●OH over Fe/N$_V$-CN disrupts mitochondrial function to induce Caspase 3 related cell apoptosis, which leads to the significant shrinkage of Cal27 cell-induced tumor. This work provides not only an effective photosensitizer for cancer therapy avoiding the accumulation of OH$^-$ but also a novel approach by the construction of dual carrier-transfer channels on semiconductor photosensitizers for improving curative effect of PDT.

CRediT authorship contribution statement

Meixian Liu: Writing – original draft, Funding acquisition, Data curation, Conceptualization. **Yuan Zhang:** Methodology, Investigation, Formal analysis, Data curation. **Fa Jiang:** Software. **Wenzhao Guan:** Resources. **Jing Cui:** Resources. **Liwei Liu:** Investigation. **Qingpeng Xie:** Data curation. **Jia Wang:** Methodology. **Shuyun Xue:** Data curation. **Jiawen Gu:** Data curation. **Zhanfeng Zheng:** Writing – review & editing. **Xiuyun Ren:** Writing – review & editing. **Xing Wang:** Writing – review & editing.

Declaration of competing interest

There are no conflicts to declare.

Data availability

No data was used for the research described in the article.

Appendix A. Supplementary data

Supplementary data to this article can be found online at https://doi.org/10.1016/j.mtbio.2024.101287.

References

[1] B. Hassannia, P. Vandenabeele, B. Vanden, Targeting ferroptosis to iron out cancer, Cancer Cell 35 (2019) 830–849.

[2] J. Ma, X. Peng, Z. Zhou, et al., Extended conjugation tuning carbon nitride for nonsacrificial H$_2$O$_2$ photosynthesis and hypoxic tumor therapy, Angew. Chem., Int. Ed. Engl. 61 (2022) 1–9.

[3] L. Fu, Y. Wan, C. Qi, et al., Nanocatalytic theranostics with glutathione depletion and enhanced reactive oxygen species generation for efficient cancer therapy, Adv. Mater. 33 (2021) 2006892–2006902.

[4] C. Huang, C. Liang, T. Sadhukhan, et al., In-vitro and in-vivo photocatalytic cancer therapy with biocompatible iridium(III) photocatalysts, Angew. Chem., Int. Ed. Engl. 60 (2021) 9474–9479.

[5] E. Murphy, A. Friedman, Hydrogen peroxide and cutaneous biology: translational applications, benefits, and risks, J. Am. Acad. Dermatol. 81 (2019) 1379–1386.

[6] J. Zhou, W. Wang, C. Zhang, et al., Ru(II)-modified TiO₂ nanoparticles for hypoxia-adaptive photo-immunotherapy of oral squamous cell carcinoma, Biomaterials 289 (2022) 121757–121771.

[7] P. Yadav, C. Zhang, A. Whittaker, et al., Magnetic and photocatalytic curcumin bound carbon nitride nanohybrids for enhanced glioma cell death, ACS Biomater. Sci. Eng. 5 (2019) 6590–6601.

[8] X. Xu, H. Zhao, J. Wang, et al., Synthesis of iron-boride/carbon-nitride composites and their applications in chemodynamic therapy, J. Colloid Interface Sci. 658 (2024) 276–285.

[9] L. Cao, Z. Feng, R. Guo, et al., The direct catalytic synthesis of ultrasmall Cu₂O-coordinated carbon nitrides on ceria for multimodal antitumor therapy, Mater. Horiz. 10 (2023) 1342–1353.

[10] M. Younis, G. He, J. Qu, et al., Inorganic nanomaterials with intrinsic singlet oxygen generation for photodynamic therapy, Adv. Sci. 8 (2021) 2102587–2102594.

[11] M. Liu, J. Liu, Z. Zeng, et al., Steric hindrance effect induced photopurification of styrene oxide over surface modified polymeric carbon nitride, Sep. Purif. Technol. 300 (2022) 121937–121937.

[12] C. Liu, Y. Cao, Y. Cheng, et al., An open source and reduce expenditure ROS generation strategy for chemodynamic/photodynamic synergistic therapy, Nat. Commun. 11 (2020) 1735–1743.

[13] H. Liu, X. Lv, J. Qian, et al., Graphitic carbon nitride quantum dots embedded in carbon nanosheets for near-infrared imaging-guided combined photo-chemotherapy, ACS Nano 14 (2020) 13304–13315.

[14] X. Zhang, O. Jeremiah, W. Pan, et al., Carbon nitride hollow theranostic nanoregulators executing laser-activatable water splitting for enhanced ultrasound/fluorescence imaging and cooperative phototherapy, ACS Nano 14 (2020) 4045–4060.

[15] H. Wang, Q. Lin, L. Yin, et al., Biomimetic design of hollow flower-like g-C₃N₄@ PDA organic framework nanospheres for realizing an efficient photoreactivity, Small 15 (2019) 1900011–1900018.

[16] Z. Yang, M. Yuan, Z. Cheng, et al., Defect-repaired g-C₃N₄ nanosheets: elevating the efficacy of sonodynamic cancer therapy through enhanced charge carrier migration, Angew. Chem. Int. Ed. 63 (2024) 1–10.

[17] X. Fang, S. Cai, M. Wang, et al., Photogenerated holes mediated nitric oxide production for hypoxic tumor treatment, Angew. Chem. Int. Ed. 60 (2021) 7046–7050.

[18] W. Dirersa, T. Kan, J. Chang, et al., Engineering H₂O₂ self-supplying platform for xdynamic therapies via Ru–Cu peroxide nanocarrier: tumor microenvironment-mediated synergistic therapy, ACS Appl. Mater. Interfaces 16 (2024) 24172–24190.

[19] T. Wachi, T. Shuto, Y. Shinohara, et al., Release of titanium ions from an implant surface and their effect on cytokine production related to alveolar bone resorption, Toxicology 327 (2015) 1–9.

[20] C. Gu, X. Liu, L. Luo, et al., Metal-DNA nanocomplexes enhance chemo-dynamic therapy by inhibiting autophagy-mediated resistance, Angew. Chem.-Int. Edit. 62 (2023) 1–10.

[21] J. Wang, L. Sun, X. Li, et al., Alkali exposure induces autophagy through activation of the MAPK pathway by ROS and inhibition of mTOR in eriocheir sinensis, Aquat. Toxicol. 258 (2023) 106481–106489.

[22] M. Liu, J. Liu, X. Gu, et al., Precisely regulating hydroxyl groups and carbon vacancies on carbon nitride for in-situ photomineralization of phenol, J. Catal. 426 (2023) 345–351.

[23] J. Cai, J. Huang, S. Wang, et al., Crafting mussel-inspired metal nanoparticle-decorated ultrathin graphitic carbon nitride for thedegradation of chemical pollutants and production of chemical resources, Adv. Mater. 31 (2019) 1806314–1806325.

[24] H. Yu, R. Shi, Y. Zhao, et al., Alkali-assisted synthesis of nitrogen deficient graphitic carbon nitride with tunable band structures for efficient visible-light-driven hydrogen evolution, Adv. Mater. 29 (2017) 1605148–1605155.

[25] M. Wang, C. Fan, S. Yang, et al., Nitrogen deficient carbon nitride for efficient visible light driven tetracycline degradation: a combination of experimental and DFT studies, Catal. Sci. Technol. 10 (2020) 6800–6808.

[26] C. Cometto, R. Kuriki, L. Chen, et al., A carbon nitride/Fe quaterpyridine catalytic system for photostimulated CO₂-to-CO conversion with visible light, J. Am. Chem. Soc. 140 (2018) 7437–7440.

[27] I. Khan, N. Baig, A. Qurashi, Graphitic carbon nitride impregnated niobium oxide (g-C₃N₄/Nb₂O₅) type (II) heterojunctions and its synergetic solar-driven hydrogen generation, ACS Appl. Energy Mater. 2 (2018) 607–615.

[28] Y. Wang, Q. Li, L. Zhang, et al., A gel-limiting strategy for large-scale fabrication of Fe–N–C single-atom ORR catalysts, J. Mater. Chem. A 9 (2021) 7137–7142.

[29] W. Oh, C. Ng, S. Ng, et al., Rapid degradation of organics by peroxymonosulfate activated with ferric ions embedded in graphitic carbon nitride, Sep. Purif. Technol. 230 (2020) 115852–115859.

[30] Q. Yang, W. Yang, F. He, et al., One-step synthesis of nitrogen-defective graphitic carbon nitride for improving photocatalytic hydrogen evolution, J. Hazard Mater. 410 (2021) 124594–124604.

[31] G. Ba, T. Huo, Q. Deng, et al., Mechanochemical synthesis of nitrogen-deficient mesopore-rich polymeric carbon nitride with highly enhanced photocatalytic performance, ACS Sustain. Chem. Eng. 8 (2020) 18606–18615.

[32] Z. Gu, Z. Cui, Z. Wang, et al., Carbon vacancies and hydroxyls in graphitic carbon nitride: promoted photocatalytic NO removal activity and mechanism, Appl. Catal. B Environ. 279 (2020) 119376–119386.

[33] J. Gao, Y. Wang, S. Zhou, et al., A facile one-step synthesis of Fe-doped g-C₃N₄ nanosheets and their improved visible-light photocatalytic performance, ChemCatChem 9 (2017) 1708–1715.

[34] X. Zhang, P. Ma, C. Wang, et al., Unraveling the dual defect sites in graphite carbon nitride for ultra-high photocatalytic H₂O₂ evolution, Energy Environ. Sci. 15 (2022) 830–842.

[35] G. Wang, Y. Zhao, H. Ma, et al., Enhanced peroxymonosulfate activation on dual active sites of N vacancy modified g-C₃N₄ under visible-light assistance and its selective removal of organic pollutants, Sci. Total Environ. 756 (2021) 144139–144151.

[36] S. Tonda, S. Kumar, S. Kandula, et al., Fe-doped and -mediated graphitic carbon nitride nanosheets for enhanced photocatalytic performance under natural sunlight, J. Mater. Chem. A 2 (2014) 6772–6780.

[37] C. Lu, X. Chen, Nanostructure engineering of graphitic carbon nitride for electrochemical applications, ACS Nano 15 (2021) 18777–18793.

[38] J. Murray, P. Politzer, The electrostatic potential: an overview, WIRES Comput. Mol. Sci. 1 (2011) 153–163.

[39] G. Meek, A. Baczewski, D. Little, et al., Polaronic relaxation by three-electron bond formation in graphitic carbon nitrides, J. Phys. Chem. C 118 (2014) 4023–4032.

[40] B. Zhao, Z. Ma, S. Ding, et al., Catalytic MnWO₄ nanorods for chemodynamic therapy synergized radiotherapy of triple negative breast cancer, Adv. Funct. Mater. 33 (2023) 2306328–2306341.

[41] W. Li, L. Chen, M. Qiu, et al., Highly efficient epoxidation of propylene with in situ-generated H₂O₂ over a hierarchical TS-1 zeolite-supported non-noble nickel catalyst, ACS Catal. 13 (2023) 10487–10499.

[42] S. Jarmelo, N. Maiti, V. Anderson, et al., Cα-H bond-stretching frequency in alcohols as a probe of hydrogen-bonding strength: a combined vibrational spectroscopic and theoretical study of n-[1-D]propanol, J. Phys. Chem. A 109 (2005) 2069–2077.

[43] M. Liu, M. Gao, L. Pei, et al., Tailoring phenol photomineralization pathway over polymeric carbon nitride with cyano group multifunctional active sites, Appl. Catal. B Environ. 284 (2021) 119710–119718.

[44] F. Wei, S. Kuang, T. Rees, et al., Ruthenium(II) complexes coordinated to graphitic carbon nitride: oxygen self-sufficient photosensitizers which produce multiple ROS for photodynamic therapy in hypoxia, Biomaterials 276 (2021) 121064–121073.

[45] J. Liu, H. Wang, R. Ye, et al., Promotional effect of Mn-doping on the catalytic performance of NiO sheets for the selective oxidation of styrene, J. Colloid Interface Sci. 585 (2021) 61–71.

[46] T. Liu, J. Li, Y. Liu, et al., SNX11 identified as an essential host factor for SFTS virus infection by CRISPR knockout screening, Virol. Sin. 34 (2019) 508–520.

[47] X. Bai, Y. Huang, M. Lu, et al., HKOH-1: a highly sensitive and selective fluorescent probe for detecting endogenous hydroxyl radicals in living cells, Angew. Chem. Int. Ed. 56 (2017) 12873–12877.

[48] T. Shen, Y. Mou, Research progress in mitochondrial dysfunction and its related diseases, Chin. Bull. Life Sci. 30 (2018) 87–93.

[49] N. Hideaki, J. Fang, M. Hiroshi, Development of next-generation macromolecular drugs based on the EPR effect challenges and pitfalls, Expet Opin. Drug Deliv. 12 (2015) 53–64.

[50] I. Melero, E. Castanon, M. Alvarez, et al., Intratumoural administration and tumour tissue targeting of cancer immunotherapies, Nat. Rev. Clin. Oncol. 18 (2021) 558–576.